Journal of Constructional Steel Research 153 (2019) 55–70

Contents lists available at ScienceDirect

Journal of Constructional Steel Research

Effects of different steel-concrete composite slabs on rigid steel beam-column connection under a column removal scenario

Junjie Wang [a,b,c], Wei Wang [a,b,*], Dawn Lehman [c], Charles Roeder [c]

[a] State Key Laboratory of Disaster Reduction in Civil Engineering, Tongji University, Shanghai 200092, China
[b] Department of Structural Engineering, Tongji University, Shanghai 200092, China
[c] Civil & Environmental Engineering, University of Washington, Seattle, WA98195-2700, USA

ARTICLE INFO

Article history:
Received 16 June 2018
Received in revised form 13 August 2018
Accepted 21 September 2018
Available online 23 October 2018

Keywords:
Disproportionate collapse
Progressive collapse
Steel moment frame
Steel deck
Catenary mechanism

ABSTRACT

Trapezoidal and Reentrant are two ordinary deck profiles in modern steel-concrete composite floor system in China. The progressive collapse resistance of rigid steel beam-column connections with these two different composite deck profiles was experimentally investigated. This research addressed progressive collapse behavior of components evaluated by removing columns through the alternate load path method where the connections simulated the behavior of connections from a multi-bay steel moment-resisting frame. Also, collapse resistance of the connection above the removed column and the adjacent connection was considered. The results were compared with a bare steel subassembly, which has the same configuration but without composite slab, the load carrying capacity of the specimen with trapezoidal steel deck is improved by 28% and the specimen with reentrant steel deck is improved by 44%. The type of steel decks influenced the degree of restraint to the beam top flange and resistance of the connection. The specimen with trapezoidal steel deck had a higher plastic rotation capacity than the reentrant one, but the specimen with reentrant steel deck had improved composite behavior in the large deformation range and, therefore, developed more catenary action than the specimens with trapezoidal steel deck. Overall, the specimens with reentrant steel deck had a better performance under the progressive collapse situation, however, some constructional measures must be made to delay the bottom beam flange fracture.

1. Introduction

Progressive collapse of structures begins with the failure of a few structural elements and then spreads to adjacent elements until substantial or complete collapse of a structure [1]. Potential causes of progressive collapse include design and construction flaws, explosion, bomb attack or some other extreme events. Design methods to prevent progressive collapse are found in the Unified Facilities Criteria, DoD [2] and the General Services Administration publication, GSA [3]. Both documents use the alternate load path method, which considers column removal as the initial damage state, and subsequently analyzes and designs the structural system to resist the demands resulting from the column removal. When a column is removed, an alternative load path capable of withstanding the full demands must be formed by the beams and slabs to redistribute the load initially supported by the removed column. Under this scenario, the response of the beam-column connections next to the removed column is crucial in sustaining and redistributing the gravity loads [4].

Prior research has investigated the behavior of steel beam-column connections under column-loss scenarios. Sadek et al. [5] conducted a coordinated experimental and numerical assessment of the performance of the intermediate steel moment frames and the special moment frames (with reduced beam section connections) under the middle column removal scenario. Compared with the intermediate steel moment frames, both ultimate resistance and failure displacement had been improved in the special moment frames, which was benefited from the contributions of reduced beam section connections. Yang et al. [6,7] compared the performance of bolted angle, shear tab and flush end plate connections under the middle column removal scenario. The bolted web angle connection had the best performance among the tested simple-connections, while the double flange and web angle connection had the highest load and rotation capacities among the tested semi-rigid connections. Li et al. [8,9], Qin et al. [10,11], Wang et al. [12] conducted tests to study the performance of different rigid beam-column connections under the middle-column-removal scenario, and they came up with a special beam-column connection to significantly improve the catenary action [11]. Li et al. [13] experimentally investigated the collapse resistance of a one-third scale one-story bare steel moment frame with fully welded beam-column connections under the middle column loss scenario and found that, at the catenary stage, more load was distributed to the strong axis columns than that

* Corresponding author at: State Key Laboratory of Disaster Reduction in Civil Engineering, Tongji University, Shanghai 200092, China.
E-mail address: weiwang@tongji.edu.cn (W. Wang).

https://doi.org/10.1016/j.jcsr.2018.09.025
0143-974X/

distributed to the weak axis columns. These tests demonstrated that the flexural action in the early stage and catenary action in large deformation stage formed the primary collapse resistance mechanism of steel beam-column connections.

In the DoD (2016) guidelines [2], floor systems are considered to be the primary structural components of carrying horizontal tie forces, only if the girders, beams, spandrels and their connections can be able to carry the required horizontal tie force until the rotation reached 0.2 rad. Guo et al. [14–16] experimentally investigated the progressive collapse resistance of one-third scale 4-baysteel-concrete composite frames with rigid or semi-rigid composite connections under the middle column removal scenario. Yang et al. [17,18] conducted a series of experiments to study the failure modes of composite shear plate and flush end-plate connections with reentrant steel deck subjected to middle-column-loss scenario, and these connections were located in a 2-baysteel-concrete composite frames with both ends restrained against horizontal movement to represent the boundary constraint provided by surrounding structural components. The composite slabs had increased the flexural and catenary resistance of both beam-column connections. Alashker et al. [19] conducted computational simulations to study the influences of slab reinforcement ratio, steel deck thickness, and shear-plate connection strength on the progressive collapse performance of composite floors, and the results indicated that the steel deck was more crucial to the collapse resistance. Besides, he suggested that the three-dimensional (3D) effect needed to consider to predict the complex collapse behavior accurately [20]. Johnson et al. [21], Hadjioannou et al. [22,23], Fu et al. [24] conducted experiments of 3D composite floors with pinned or semi-rigidbeam-column connections subjected to column loss and demonstrated the critical role of the composite slab in developing an alternate load path. Up to now, very little research has concentrated on the collapse resistance of composite structures with rigid beam-column connections and the influence of different deck profiles, including commonly used trapezoidal or reentrant steel deck, on the collapse resistance. In this experimental research, the behavior of composite beam-column connections in a middle-column-removal scenario has been investigated.

2. Experimental scheme

2.1. Test specimen

The test specimens for this experimental research were based upon the prototype moment-resisting steel frame building with composite floors shown in Fig. 1(a). The girder and beam span lengths are 4.5 m and 6 m, respectively. 5 kN/m^2 dead load (DL) and 2 kN/m^2 live load (LL), typical office building gravity loading, were used to design this floor system. The ASCE/SEI 7-16 (2017) [25] load combination for extreme events 1.2DL + 0.5LL ($1.2 \times 5 + 0.5 \times 2 = 7$kN/m^2) was used for the post-column-lossload-carrying evaluation.

The test subassembly was essentially a plane section as shown in the Fig. 1(a). After the middle column was removed, only the contribution of girders which connected to the column was considered, and the contribution of transverse beams connecting to the column was neglected. This neglect would underestimate the resistance of the prototype structure, because the transverse beams could develop extra vertical resistance in the direction orthogonal to the girder. However, one of the primary objectives of this research is to investigate the behavior the moment-resisting connection under the column removal scenario. If both girder-to-column connection and beam-to-column connection were moment-resisting connection, the combined behavior of girder and beam would be similar with that of the neglecting-beam specimen. In this sense, the simplification mentioned before would not affect the tendency of the collapse behavior too much. Besides, the prototype structure was designed by the strong column-weak beam principle. Thus, the column would be intact during the progressive collapse process. The transverse beam could not affect the behavior of the girder-to-column connection. For convenience, the term 'girder' will be replaced by 'beam' in the rest of this paper. The beam-column connections

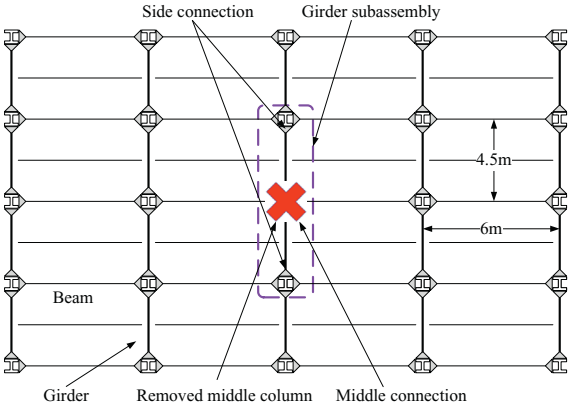

(a) Plane view of prototype building

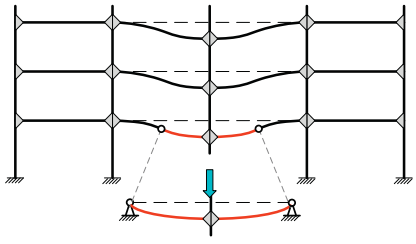

(b) Middle connection

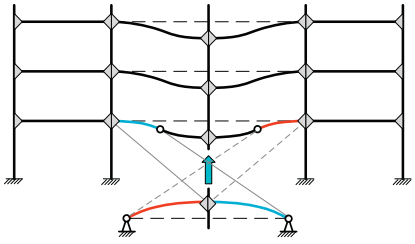

(c) Side connection

Fig. 1. Prototype composite girder-column subassembly.

Table 1
Summary of test specimens.

Specimen	Loading condition	Deck type	Connection type	Beam section	Longitudinal rebar	Transverse rebar	Shear stud
ST-M-R	Middle joint	Reentrant	Welded flage - bolted web connection	H300 × 150 × 6 × 8 (mm)	Φ 10 @ 200	Φ 6 @ 200	Diameter(19 mm); Height(80 mm); Space(250 mm)
ST-M-T		Trapezoidal			Φ 10 @ 200	Φ 6 @ 200	
ST-S-R	Side joint	Reentrant			Φ 10 @ 200	Φ 6 @ 200	
ST-S-T		Trapezoidal			Φ 10 @ 200	Φ 6 @ 200	

were fully restrained, and so an inflection point is approximately located at the midpoint of the beam span, as illustrated in Fig. 1(b)and (c). In an actual structure, this inflection point will move during the progressive collapse and is not precisely at the midpoint of the beam span [17,18]. However, for the sake of comparing the performances of different types of composite joint subassemblies, it was deemed reasonable to make this assumption, since it was desirable to keep the geometry and boundary conditions of the tests identical. Furthermore, this simplification also facilitates the comparison of the measured structural responses between a previous steel subassembly test (Specimen ST-WB in the paper by Wang et al. [12]) and these composite test specimens.

As shown in Fig. 1(b)and (c), two types of composite subassemblies were tested. The middle connection subassembly (Fig. 1(b)) located above the lost column was tested in sagging or positive moment, and the side connection subassembly (Fig. 1(c)) evaluates the adjacent single cantilever beam connection in negative bending. The side connection assembly is tested as a simple span with an upward load to create negative bending, while the middle span has a downward load for positive bending. As shown within the dashed lines in Fig. 1(a), the possible failure behavior of the double-span subassembly could be partially reflected by these two specimen types.

Four specimens were designed to investigate the behavior of the middle and side connections with composite slabs on reentrant (R-185-740) and trapezoidal (T-250-750) metal deck. Each specimen had two H-section beams (H300 x 150 × 6 × 8 mm) with composite slab (700 mm wide, 100 mm thick) and a vertical HSS section stub column (250 × 14 mm), located at the center of the specimen. Table 1 provides detailed information about these test specimens.

The dimensions and connection details of every specimen are shown in Fig. 2. Welded flange-bolted web connections were used in these

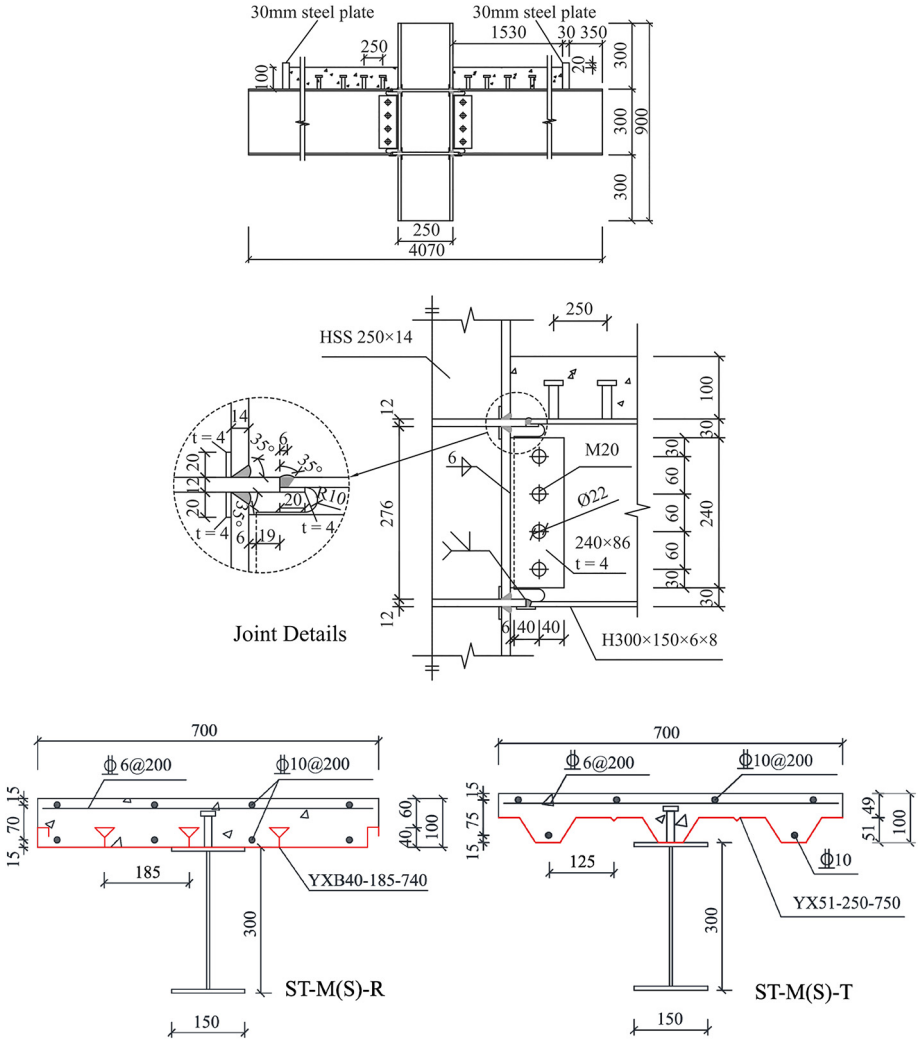

Fig. 2. Specimen details.

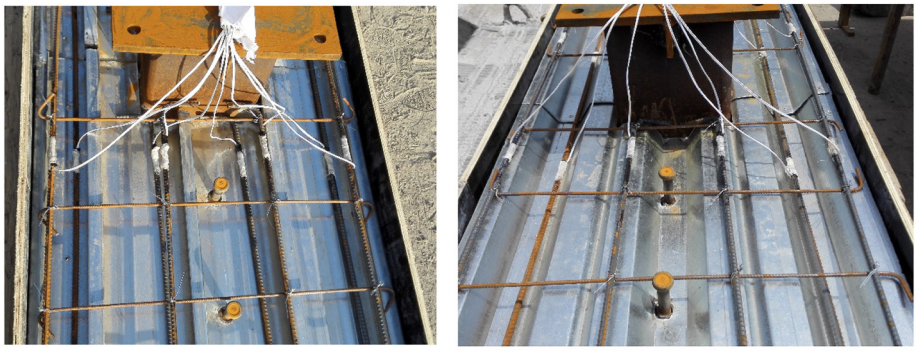

(a) ST-M(S)-R (b) ST-M(S)-T

Fig. 3. Photos of specimens.

specimens, in which full penetration welds were used to connect the beam flanges to the through diaphragms (12 mm) of the column. For the bolted shear-plate beam web joints, four M20 Grade 10.9 slip-criticalhigh-strength bolts were used with a 155kN preload. Each beam had one row of shear studs (19 × 80 mm) with a 250 mm spacing to achieve 50% partial composite action. As shown in Fig. 2, the spacing of the slab reinforcement was 200 mm in each direction. To simulate the continuous boundary conditions of the composite slabs, two 30 mm-thick steel end plates were welded to the beam flanges to restrict both sides of the composite slab, and the longitudinal reinforcement was welded to the steel plates.

To facilitate construction, the profiled steel decks were cut into two parts at the joints, then connected with aluminum rivet, which had negligible shear resistance, at the middle of the specimen as shown in Fig. 3. The specimen designation is as follows: ST-M(*S*)-R(T), where ST represents the HSS column stub with through diaphragm, M is a middle connection, S indicates a side connection, R represents the reentrant steel deck, and T represents the trapezoidal steel deck.

The specimens were made with Q345-grade steel, C30-grade concrete and HRB400 reinforcing steel bar. The results of material tests are provided in Table 2. The compressive strengths of concrete were 36.33 MPa for ST-M(*S*)-R and 41.15 MPa for ST-M(*S*)-T, which were determined using standard 150 mm × 150 mm × 150 mm cubes and were conducted at the day of the test. High-strength Grade 10.8 (ultimate tensile strength = 1000 MPa, yield-tensile ratio = 0.8) bolts were used for all specimens. The material properties of the bolts were the nominal values provided by the manufacturer. Tension tests were not performed on the steel decks and shear studs, and the standard yield strengths of 250 MPa and 320 MPa in accordance with the Chinese building codes [26,27] were employed.

2.2. Test setup

The test setup is shown in Fig. 4. The overall length of each specimen was 4.5 m. A horizontally self-equilibrating frame was designed to simulate the boundary constraint provided by surrounding structural components. The specimens were supported by pins at the ends of the beam. A vertical guide was provided at the center of the test setup to provide rotational restraint, so that the stub could only be moved along the vertical direction. Adisplacement-controlled point load was applied to the vertical stub. The primary difference in the middle and side column subassemblies was the direction of loading, as indicated in Fig. 1b and c. 500 mm stroke actuator was used in this test. The load was applied at a rate of 5 mm/min before the fracture of steel beam flange. Afterward, the loading rate changed to 8 mm/min. The test terminated when the beam-column joint had been completely ruptured, or the stroke of the actuator was reached.

Table 2
Material properties.

Steel type	f_y (MPa)	f_u (MPa)	Ultimate strain
Column	482	545	24%
Beam Flange	387	441	31%
Beam Web	417	514	27%
Longitudinal bar	527	699	22%
Transverse bar	537	754	28%
Concrete (Re-entrant)		36.33	
Concrete(Trapezoidal)		41.15	

2.3. Instrumentation

Fig. 5 shows the instrumentation layout for the specimens. The applied point load was measured by the built-in load cell of the actuator. A total of 16 displacement transducers measured the vertical deflections of beams and possible movements of the supports. The vertical and horizontal displacement transducers were represented by 'V' and 'H'; respectively in Fig. 5(a).

As shown in Fig. 5(b)and (c), strain gauges were attached to 3 beam sections (W1/E1, W2/E2, and W3/E3) to monitor their strain distributions. During the test, the strain of the W1/E1 section will remain in elastic range, therefore, the moment and axial force of this section could be explicitly calculated by linear elastic behavior and equilibrium. The strains over the critical sections, W2/E2 and W3/E3, were measured to monitor the strain distribution near the location where connection fracture was expected. Concrete surface strains and strains in reinforcing bars were monitored at the W2/E2 section, as shown in Fig. 5d and e.

3. Experimental results

3.1. Failure modes

3.1.1. Middle connection tests

The measured vertical load-displacement response (at midpoint) of the four specimens and the comparable bare steel specimen are shown in Fig. 6. The vertical displacement, δ, is the average of the vertical displacements measured by instruments V1 and V2 (Fig. 5). The beam chord rotation θ is calculated by dividing δ by the length of half-span(2250 mm). The bottom beam flange of the steel subassembly, identical to the composite specimens but without slab, fractured at a displacement of 74 mm, and achieved a maximum load of 184kN. Then, after the other side bottom beam flange fractured, the axial resistance by the remaining connection provided catenary action. When the displacement reached 381 mm, the ultimate load 218kN was achieved, and the whole beam connection fractured, and the specimen lost its load carrying capacity.

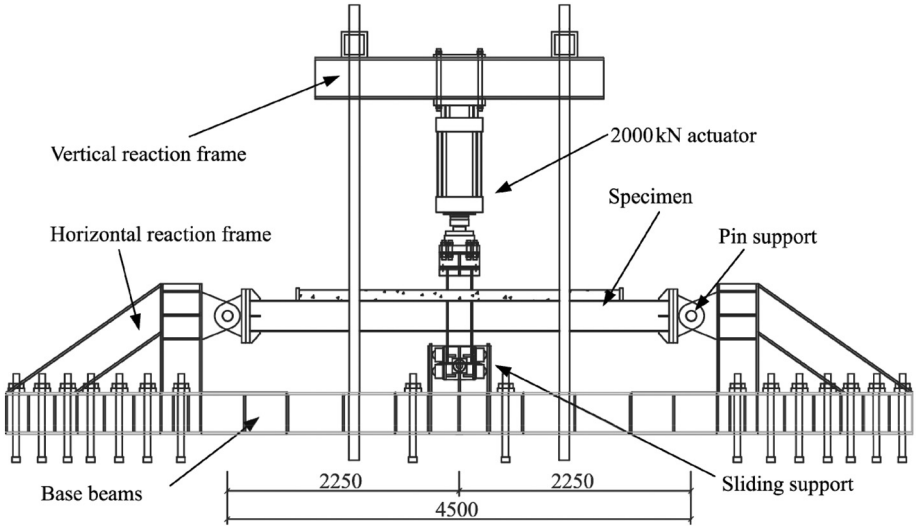

Fig. 4. Test set-up.

For the ST-M-R specimen, at a displacement of 23 mm (θ = 0.01 rad, F = 246.1kN), nonlinearity was observed in the load-displacement response. At a displacement of approximately 30 mm (θ = 0.013 rad, F = 282 kN), cracks were observed at the concrete slab around the column. Following the peak load (324 kN) at the displacement of 53 mm (θ = 0.024 rad, Point A), the bottom beam flange of section W3 fractured (Fig. 7(a)), but, buckling of the top beam flanges was not observed (Fig. 7(b)). As the displacement increased further, the vertical resistance exhibited a continued increase until displacement reached 171 mm (θ = 0.076 rad). At this point, the vertical resistance achieved its local maximum load (288kN). During this period, the cracks of the concrete slab mainly localized near the steel column (Fig. 7(c)). When the displacement reached 185 mm (θ = 0.082 rad, F = 267 kN, PointB), the bottom beam flange of E3 section suddenly fractured (Fig. 7(d)) and the vertical resistance dropped to approximately 100kN. Meanwhile, west beam web shear-plate net section cracked at the bottom edge. With increased displacement, the resistance gradually increased, apart from the slight decrease resulting from fracture of the shear plate connected to the east beam (350 mm, θ = 0.156 rad, 155kN, Point C). After the displacement reached 400 mm (θ = 0.178 rad, F = 132.2 kN, Point D), the vertical resistance rapidly increased, but the cracks in the shear plates grew longer at the same time. At a 485 mm displacement (θ = 0.216 rad, Point E), the test was terminated because the specimen touched the sliding support, with the vertical resistance at its local maximum value (307 kN). At the end of the test, cracking and tearing in the two shear plates had progressed to the lastbolt hole but the upper flanges of both beams remained intact (Fig. 7(e)). The cracks of the concrete slab were mainly located near the beam-column connection (Fig. 7(f)).

The behavior of specimen ST-M-T was similar to ST-M-R in the earlystages, noticeable nonlinear behavior and flexural cracking of theconcrete appeared at the displacement of 25 mm (θ = 0.011 rad, F= 246.4kN) and 30 mm (θ = 0.013 rad, F = 256.8 kN), respectively. At 52 mm (θ = 0.023 rad, Point F)displacement, ST-M-T reached its peak load (279kN), and tiny cracks were observed at the bottom beam flange of section W3 (Fig. 8(a)). At this point, as shown in Fig. 8(b), the trapezoidal steel deck had separated from the concrete slab at the joint area, and the rivet connection was also failed. Furthermore, the east slab end plate was bent due to the large compressive force in the concrete slab (Fig. 8(c)). With the increasing vertical displacement, local buckling was observed at the upper beam flange at E3 and the adjacent steel deck (Fig. 8(d)). This buckling was not observed in the test of ST-M-R. At the same time, the vertical resistance gradually decreased following the slow growth of the bottom beam flange cracking at section W3. When the displacement reached 130 mm (θ = 0.058 rad, F = 219 kN, Point G), the bottom beam flange at W3 fractured, which led to a sudden drop in the load-displacement curve. At this point, tiny cracks were observed in the bottom beam flange at E3 (Fig. 8(e)). The resistance increased with increasing displacement until a displacement of 230 mm (θ = 0.102 rad, 200kN, Point H)where the bottom beam flange fractured at E3 and a sudden decrease in load occurred. After this sudden decrease, the vertical force increased with increasing deflection even as crack growth continued in the shear plates. At a 450 mm displacement (θ = 0.200 rad, 240kN, Point I), the test was terminated, because the deformed trapezoidal steel deck touched the sliding support. At the end of the test, shear plate cracking had progressed to the last bolt hole at the section W3 and E3 (Fig. 8(f)). The upper flanges of both beams had been straightened and remained intact. The severe separation between the concrete slab and the metal deck was observed (Fig. 8(g)).

3.1.2. Side connection tests

For ST-S-R, flexural cracks (not limited to the connection area) were observed in the concrete slab at 30 mm (θ = 0.013 rad, F = 206.4 kN) displacement. At 60 mm (θ = 0.027 rad, F = 240 kN) displacement, as shown in Fig. 9(a), local buckling was observed at the bottom beam flange of both beams, but buckling was more severe at the W3 section. When the vertical force reached its peak load (314 kN) at a displacement of 154 mm (θ = 0.068 rad, Point J), the upper beam flange at E3 fractured which led to a sudden drop in the load-displacement curve (Fig. 9(b)). Subsequently, with increasing displacement, the vertical force increased again until the upper beam flange at W3 fractured at a displacement of 260 mm (θ = 0.116 rad, Point K)with a local maximum resistance of 310 kN (Fig. 9(c)). At a 289 mm (θ = 0.128 rad, F = 210 kN, Point L)displacement, the top layer steel rebar at the south side fractured (Fig. 9(d)), while the other rebars were no longer held in place due to spalling of the concrete, and they were sliding down into the bent reentrant steel deck and were straightened as strings (Fig. 9(e)). With further increases in displacement, the vertical force kept increasing until the bottom beam flange at W3 fractured at a displacement of 389 mm (θ = 0.173 rad, Point M)and a local maximum resistance of 310.4 kN was achieved. The loading process terminated at this point and the cracks developed in beam webs was illustrated in Fig. 9(f). The composite slab was severely damaged. Following the straightening of steel rebars, the concrete experienced progressively severe spalling, and the reentrant steel deck was bent under compression.

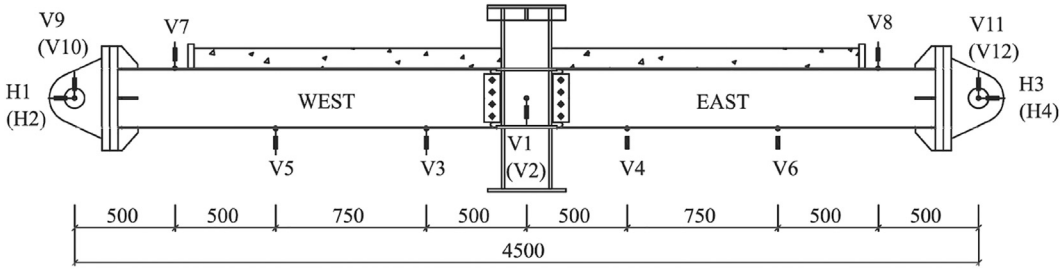

(a) Arrangement of displacement transducers

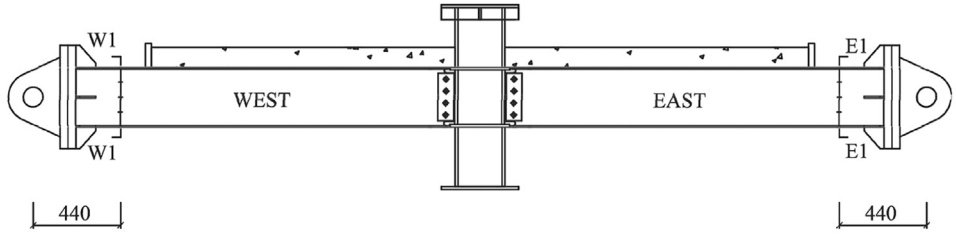

(b) Arrangement of measured strain sections

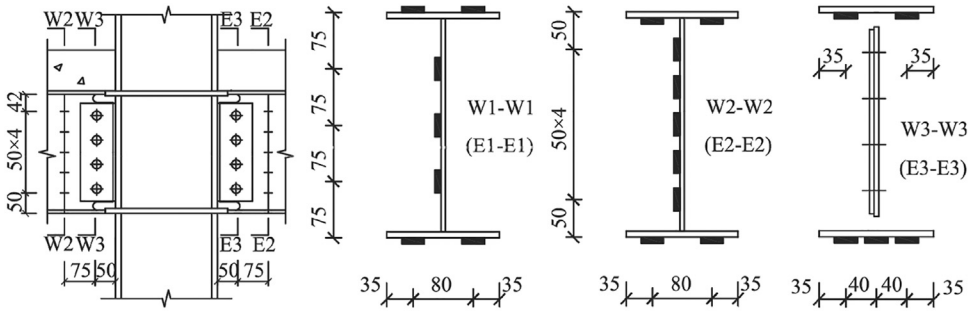

(c) Strain gauge arrangement at each section

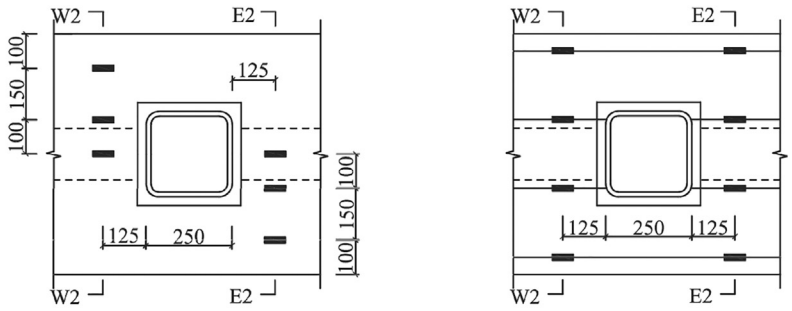

(d) Strain gauge arrangement for surface gages (plan view) (e) Strain gauge arrangement for reinforcement

Fig. 5. Layout of the instrumentation.

Specimen ST-S-T had similar behavior to ST-S-R. At a displacement of 30 mm (θ = 0.013 rad, F = 191 kN), widespread flexural cracks were observed in the concrete slab. At a displacement of 53 mm (θ = 0.024 rad, F = 225.5 kN), local buckling was observed at the bottom beam flange of both beams but was more severe at W3 (Fig. 10(a)). When the vertical force reached its peak load (311 kN) at a displacement of 180 mm (θ = 0.080 rad, F = 311.1 kN, Point N), the upper beam flange of E3 fractured (Fig. 10(b)), which led to a sudden drop in the load. Compared with ST-S-R, more severe damage, separation, and deformation in the composite slab was noted. As shown in Fig. 10(c), the trapezoidal steel deck was bent under the compression from the straightened longitudinal steel rebar, and at the same time,

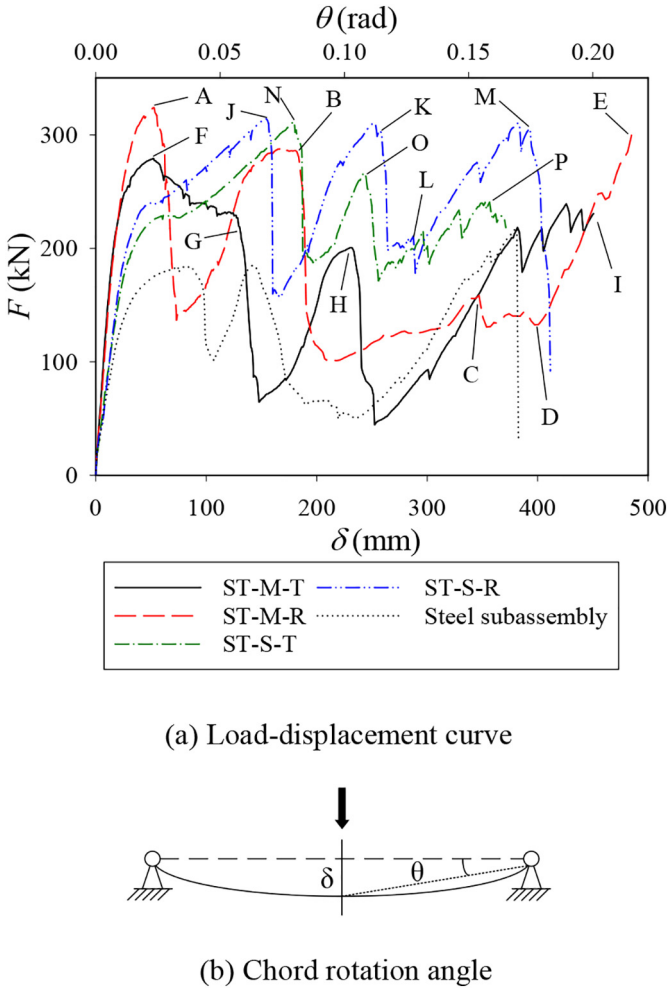

Fig. 6. Load-displacement curves of specimens.

without the support from the slab, the longitudinal rebar sliding down along the bent steel deck and could not develop tensile force necessary for flexural and catenary resistance. Subsequently, the vertical force increased with increasing deflection until the upper beam flange at W3 fractured at a displacement of 245 mm ($\theta = 0.109$ rad, F = 267kN, Point O). After the second drop, the vertical force did not increase due to the continued crack growth in the shear plates and severe spalling of the concrete (Fig. 10(e)). The bottom beam flange of W3 fractured at a displacement of 354 mm ($\theta = 0.157$ rad, Point P), and the test was terminated at a locally maximum force of 241 kN. The cracks in the shear plates were illustrated in Fig. 10(f).

3.2. Deformation pattern and corresponding deformation limits

The deformed shapes of ST-M-T and ST-S-T during the test process are plotted in Fig. 11. The deflection curve at the early stages exhibited a typical flexural mode, but as the vertical displacement increased, the deformation gradually concentrated at the connection. At the largest deformation, the beams connected to the center stub were stretched as two straight lines, and the beam-column connection deformed like a hinge. The specimens with reentrant steel decks displayed nearly identical behavior. Characteristic deformation limits and relative vertical resistances were identified from the load-displacement curves, as listed in Table 3. Before displacement reached 300 mm, because each side of the beam-column connection cracked at different deformations, every specimen had two peak loads. For specimen ST-S-T(R), the primary flexural stage ended at about the same deflection limit of approximately 0.12 rad regarding the chord rotation, but for the specimen ST-M-T and ST-M-R, the chord rotation angle is 0.11 rad and 0.08 rad, respectively. Except for the steel specimen, the peak loads in the flexural stage in Table 3 were all greater than that in the catenary action stage.

As mentioned in Section3.1, the two middle specimens were halted before the complete failure had been achieved, while the two side specimens experienced a complete failure. Thus, for the side specimens, the ultimate tensile catenary resistance could not exceed the maximum flexural resistance. However, for the middle specimens, this conclusion could not be reached, as the load-displacement curves beyond the halted points were unknown. Two reasons were lead to the inapparent tensile catenary action: 1)The rivet lap connection (Fig. 3) could not transfer tensile force, therefore, the steel deck could not directly contribute to the tensile catenary action; 2)The tensile force could not be fully developed in the steel bars as the excessive concrete spalling nearby the column, especially in the side specimens. Thus, in this test, the composite slab could not wholly contribute to the tensile catenary action.

3.3. Strain measurement

The measured strains at section W1 of the four specimens are plotted in Fig. 12. For the middle connection specimens, ST-M-R and ST-M-T, E1 sections represented flexural behavior when the displacement less than 50 mm ($\theta = 0.022$ rad), with the compression in top flange and tension in bottom flange, which indicated the resistance mainly came from the bending of the composite beam. For displacements less than 50 mm, the compressive strain in the beam top flange is of larger magnitude than the tensile strain in the beam bottom flange, demonstrating a noticeable compression bending characteristic, which was resulting from the compressive arch action, which will be discussed later. With the ascending of the displacement, the overall trend was the transformation from compression bending state to tension bending state, and finally, all the strains at the E1 section turned into the tensile strain. When the beam bottom flanges fractured at the W3/E3 sections, obviously declining of strains could be observed at the beam flanges. Afterward, the strain of the bottom beam flanges at section E1 remained stable, while the strain of the top beam flanges rapidly increased and exceeded the bottom flange in the final stage. It should be noted that the strain critical point of reverse from negative to positive of the beam top flange at E1 section was markedly different in these specimens: 210 mm ($\theta = 0.093$ rad) for ST-M-T and 360 mm ($\theta = 0.160$ rad) for ST-M-R.

For the side connection specimens, ST-S-R and ST-S-T, the evolution process of the strain at the E1 section were different from the middle connection specimens. With the top beam flange in tension and the bottom beam flange in compression, Strains at the E1 section exhibited flexural behavior at the small deformation stages. The fracture of top beam flanges at the loading joint induced apparent decreases of strain in the top beam flange. With the increase of displacement, all the strains at the E1 section were in tension, and the strains in bottom beam flange exceeded the top beam flange in the final stage. Overall, ST-S-R and ST-S-T shared similar strain evolutions characteristic at the E1 section, however, when it came to an end, the overall stress state of ST-S-R was higher than ST-S-T.

For the middle connection specimens, the concrete in the composite slab was under compression, and its compressive strength was utilized. Fig. 13 depicted the development trend of the concrete strain at the E2 section of the middle joint specimens. Overall, the ST-M-R developed higher compressive strain in concrete than ST-M-T. The concrete compressive strain of ST-M-T achieved its peak value while displacement came to 50 mm ($\theta = 0.022$ rad), then rapidly descended to about 4×10^{-4}, and kept this smaller value till the end of the test. When it came to ST-M-R, only slight reductions in the compressive strain of concrete were noted when flanges fractured at W3 and E3, and concrete strain eventually stabilized to a relatively high value till the end of the

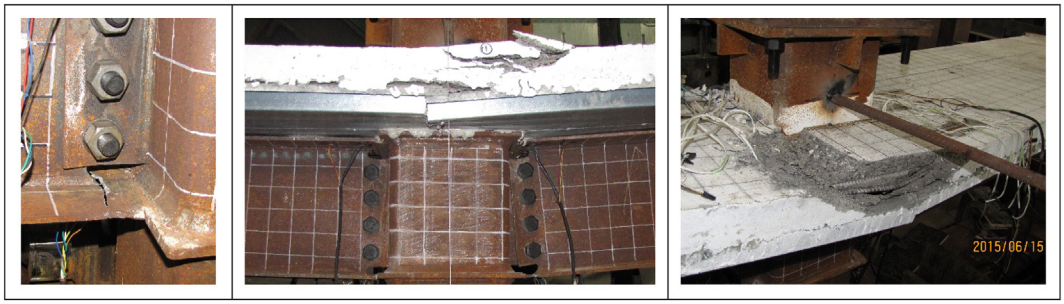

(a) flange fracture at W3 section (θ=0.024rad) (b) top beam flange (θ=0.024rad) (c) concrete cracks (θ=0.076rad)

(d) flange fracture at E3 section (θ=0.082rad) (e) shear plates (θ=0.216rad) (f) final state (θ=0.216rad)

Fig. 7. Failure modes of ST-M-R.

test. These phenomena resulted by the different cross-section shapes of steel decks, which will be discussed later.

4. Discussion of experimental results

The resistance from the catenary action and flexural action could be statically defined by the moment and shear force in the W1/E1 section, which could be calculated using the strains in these sections [28]. The response of the specimens could be idealized as two phases. In the first phase, namely flexural stage, the load is resisted by flexure of the composite section, and compressive arch action was developed in the middle joint specimens. The second stage, namely catenary stage, which occurred under the large deformation, the vertical load was resisted primarily by a catenary mechanism, with tension being carried by in the beam.

4.1. Structural response curve

The measured load-displacement curves of the four specimens are plotted in Fig. 6(a). The maximum bearing capacity at flexural stage and catenary stage of each specimen is listed in the Table . 3. The result shows that the load resistance and the initial stiffness of the specimens with composite slab are significantly higher compared with the steel subassembly. While the ultimate bearing capacity of the steel subassembly is achieved at the catenary stage, the four composite subassemblies are achieved at the flexural stage. Compared with the steel subassembly, the percentage improvement of the maximum bearing capacity for each composite specimen are ST-M-T 28%, ST-M-R 48.6%, ST-S-T 42.7%, ST-S-R 44%. The maximum bearing capacity is achieved at a lower rotation of 0.024 rad for the M specimens. The S specimens sustained a markedly strengthening process in the flexural period until the rotation angle is up to 0.068 rad.

For the M specimens, the ST-M-T and ST-M-R behave significantly different from each other among the entire load process, which is shown in Fig. 6(a). At the flexural stage, as shown in Fig. 8(a), the limited contact area between beam flange and trapezoidal steel deck lead to severe local buckling in the top beam flange of the ST-M-T, which improved the rotation capacity of the beam section, then the fracture of the bottom beam flange has been delayed. However, for the specimen ST-M-R, the reentrant steel deck could tightly restrict the top beam flange from buckling as shown in Fig. 7(a), which result in the earlier fracture in the bottom beam flange. However, because the cross-sectional area of the composite slab of ST-M-R is larger than ST-M-T, the resistance at the flexural stage of ST-M-R is higher.

At the catenary stage, the catenary action is developed at a lower rotation in ST-M-T which is similar to the steel subassembly as shown in Fig. 6(a), while higher catenary resistance was achieved in ST-M-R. As illustrated in Fig. 14, the catenary force T in ST-M-R was partially offset and delayed by the compressive force C_c developed in the composite slab as following:

$$T = T_s - C_c \tag{1}$$

Where T is the tensile axial force in the steel beams connected to the pin supports, T_s is the tensile axial force in the steel beam nearby column, C_c is the compressive force in the composite slab. With the increase of displacement, the composite slab would separate from the steel column, then C_c would diminished to a tiny level and the catenary force would equal to the tensile axial force at the steel members [28]. Because the severe damage of the concrete slab in the ST-M-T, the C_c could be neglected, then the catenary action is emerged similar with steel subassembly as shown in Fig. 6(a). Moreover, the reinforcement near the connection of ST-M-T could not be tightly restricted due to the severe damage of the concrete slab, which lead to limited catenary action was provided by the reinforcement, then the ultimate catenary resistance of ST-M-T is lower than ST-M-R.

For the S specimens, as indicated in Fig. 6(a), similar behavior is observed in the flexural stage. This is because the concrete slab is in tension for these specimens and the effect of concrete could be neglected, then the section properties of the two specimens are similar to each

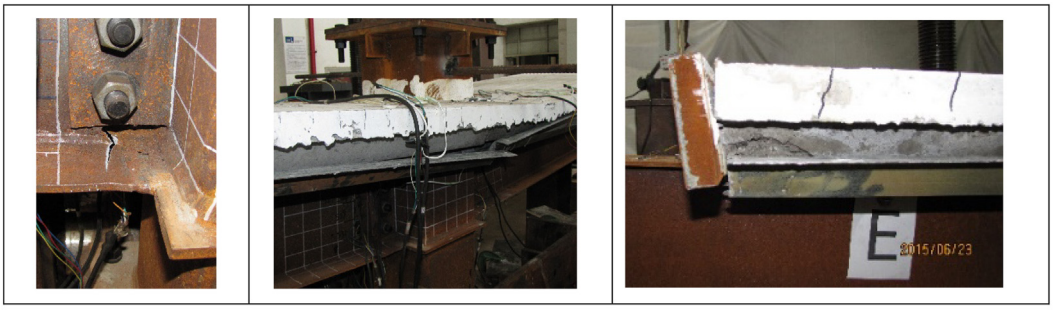

(a) crack at W3 section (θ=0.023rad) (b) deck separation (θ=0.023rad) (c) bent slab end plate(θ=0.023rad)

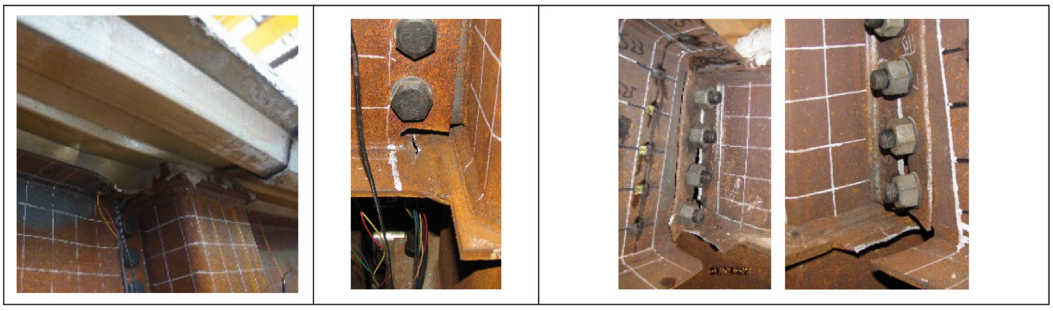

(d)local buckling (θ=0.045rad) (e) crack at E3 section (θ=0.058rad) (f) shear plates (θ=0.200rad)

(g) final state (θ=0.200rad)

Fig. 8. Failure modes of ST-M-T.

other. However, the force in the catenary phase is higher for Specimen ST-S-R; this difference results from different degeneration degree of the composite slabs. The inverted triangle in the reentrant steel deck could improve the composite effect of the slab and prevent the damage of concrete slab; then the reinforcement develops more catenary action. As shown in Fig. 9(d), the fracture of the reinforcement demonstrated the axial force had been fully developed, however, because the severe slab damage of ST-S-T, no reinforcement fracture was exhibited in this specimen. Besides, the reentrant steel deck could supply more support to the shear studs than the trapezoidal steel deck. Therefore, the composite action between steel beam and composite slab was better in ST-S-R, which could also benefit to the reinforcement develop more tensile force. Furthermore, the ST-S-R has eight longitudinal reinforcements, while ST-S-T only has six, which would also affect the catenary force.

As the middle connection specimen and side connection specimen were generated from the same moment frame, it is critical to know how the frame behaves under middle column removal scenario. As shown in Fig. 15(a), in a practical situation, with the force F imposed to the middle column, the middle connection and side connection will conjoint sustain the same load. Based on this premise, the chord rotation angle of the complete connection subassembly could be derived by the chord rotation angle of middle connection specimen and side connection specimen under the same vertical load, that is $(\theta_1 + \theta_2)/2$. However, if the vertical load surpassed either first peak load of middle connection specimen or side connection specimen, there must be involved in a complicated unloading process for the other specimen, furthermore, greater tensile axial force at the catenary stage may also significantly affect the behavior of connection resistance, which may not be able to generate reasonable results. In this sense, only the behavior before the first peak load was considered. Thus, the F-θ relations of complete connection subassembly with reentrant deck (represent by R-full) and complete connection subassembly with trapezoidal deck (represent by T-full) were illustrated in Fig. 15(b). The peak load and relative chord rotation angle of R-full are 314 kN and 0.043 rad, while that are 279 kN and 0.044 rad for T-full. By this mean, the flexural peak load of R-full is 12.5% than T-full, but they will achieve this peak load at almost same displacement.

4.2. Compressive arch action

Fig. 16 depicts the axial force development at the E1 section of the specimens. The axial force was calculated by the measured strain of the E1 section. At the flexural stage, there were many differences

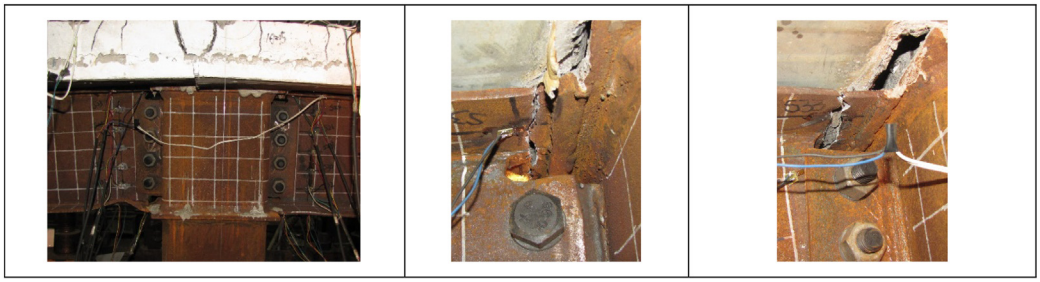

(a) local buckling (θ=0.027rad) (b) fractured beam flange (E3) (θ=0.068rad) (c) fractured beam flange (W3) (θ=0.116rad)

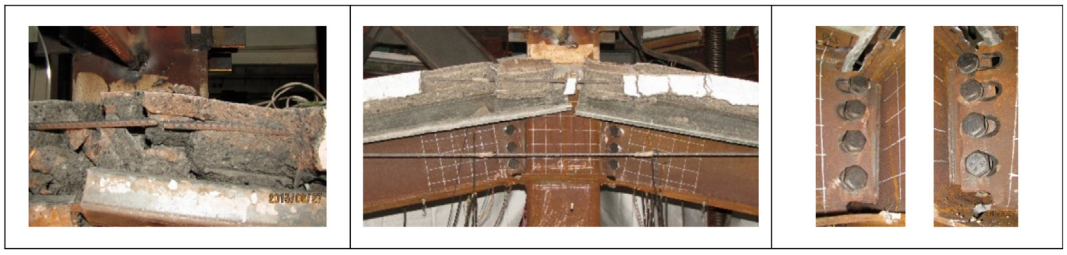

(d) ruptured rebar (θ=0.128rad) (e) straightened rebar (θ=0.173rad) (f) beam web (θ=0.173rad)

Fig. 9. Failure modes of ST-S-R.

between middle connection specimens with side connection specimens. The side connection specimens shared many similarities with each other, including the kept increasing trends of the axial force apart from some tiny drop caused by beam flange fracture, and what's more, the axial force in the beam always be tensile. When it came to middle connection specimen, a marked compressive stage can be pointed out at the initial stage, especially ST-M-R. The reason for this is that, due to the design of the specimens, the neutral axis in the composite beam close to the joint area was higher than it in the fixed pin joints, which led to a compressive arch action. As shown in Figs.17 and 18, near the pin support, the neutral axis was located at the center of the steel beam, but at the beam-column connection area, the neutral

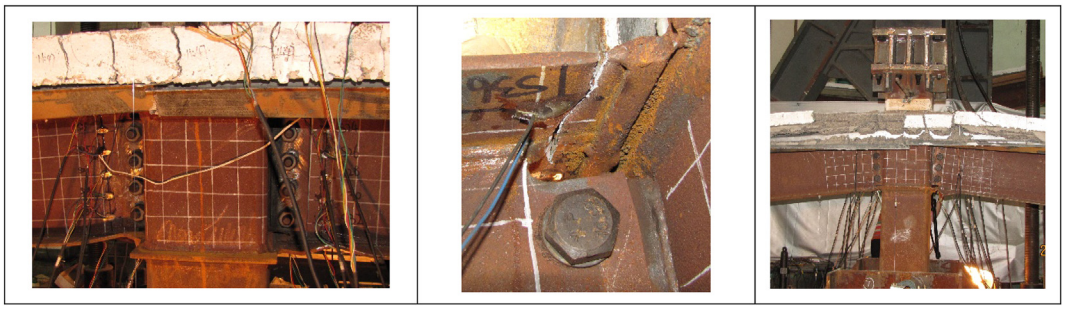

(a) local buckling (θ=0.024rad) (b) fractured beam flange(E3) (θ=0.080rad) (c) composite slab (θ=0.080rad)

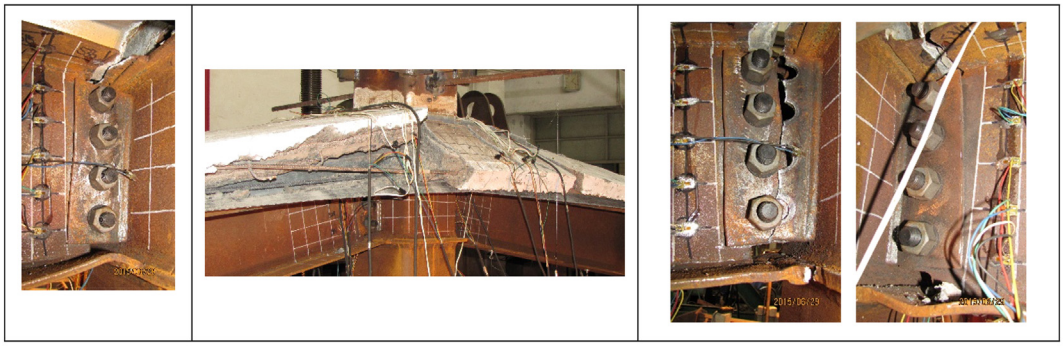

(d) fractured beam flange(W3) (θ=0.109rad) (e) damaged composite slab (θ=0.157rad) (f) shear plates (θ=0.157rad)

Fig. 10. Failure modes of ST-S-T.

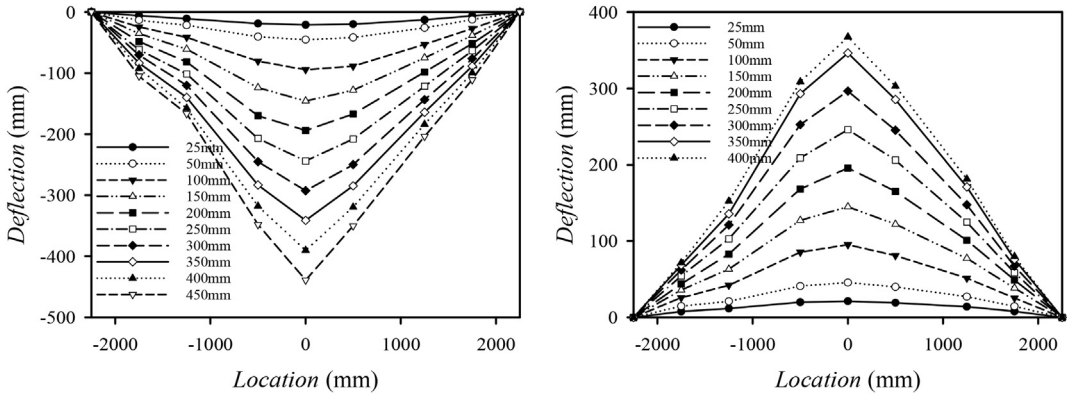

Fig. 11. Deformation patterns of ST-M-T and ST-S-T.

axis was close to the top beam flange, then the δ in Fig. 18 could represent this height difference.

Assuming that the middle connection specimen would keep intact in the load process, then, there will be three unique states as shown in Fig. 18. The blue curve represents state 1, which is generated from the initial state as shown in Fig. 17. At this state, the specimen does not have any axial force, but, if there is any small vertical displacement, due to the fixed pin support, the compressive axial force will emerge and increase with the displacement. When the vertical displacement equal to δ (state 2), the neutral axis height difference between beam ends and the connection area, the maximum compressive axial force will be attained. As the displacement keep increasing, the compressive axial force will decrease. Because the hypothesis of the specimen will keep intact, when the vertical displacement reaches 2δ, which is state 3, the compressive axial force will be decreased to zero. After that, the axial force will be changed to tensile. For ST-M-R and ST-M-T, the δ is 142.6 mm and 133 mm, respectively. That means the state 2 and state 3 for ST-M-R are 142.6 mm and 285.2 mm, while that are 133 mm and 266 mm for ST-M-T. Back to Fig. 16, the corresponding displacements at the maximum compressive force and transformation point from compression to tension are 86 mm and 268 mm for ST-M-R, while those are 49 mm and 85 mm for ST-M-T. Obviously, ST-M-R is closer to the hypothesis than ST-M-T, which imply the degeneration of the slab in ST-M-R is less than ST-M-T. Therefore, the compressive arch action was much prominent in the ST-M-R. As shown in Figs.7 and 8, the concrete damage in ST-M-T was more severe than that in ST-M-R, which led to the compressive force generated in ST-M-T was much smaller than that in ST-M-R. What's more, the height of the neutral axis at the joint area would descend simultaneously as the damage developed in the concrete slab. With the descending of the neutral axis in the joint area, the compression-tension transfer point was much earlier in ST-M-T. In the test conducted by Yang [18], the compressive arch forces were also decreased due to the excessive damage in the concrete slab. The different damage degrees in these two specimens mainly attributed to the different steel deck cross-section shapes of these specimen, which will be discussed in the following section. As the displacement kept growing, the compressive arch action diminished which can be indicated from the decreasing in the compressive axial force. Finally, catenary action could be generated to resist the vertical load when the axial force turned into tension.

4.3. Contributions of flexural actions and axial force effects

The vertical resistance F was contributed by the flexural action and axial force effect, which included compressive arch action and tensile catenary action. As shown in Fig. 19, the vertical load resisted by axial force effect (FA) could be derived by Eq.(2). The axial forces N_1 and N_2 are shown in Fig. 16. Then, the vertical load resisted by flexural action (FF) could be defined by Eq.(3).

$$FA = N_1 \sin\theta + N_2 \sin\theta \tag{2}$$

$$FF = F - FA \tag{3}$$

The vertical loads carried by FA and FF are plotted in Fig. 20. For the middle joint specimens, the vertical loads were almost wholly resisted by the flexural action before the fracture of the bottom beam flange. After the fracture of both side bottom beam flange, the catenary action started to be mobilized and eventually exceeded the resistance of flexural action. For ST-M-R, an apparent compressive arch action was formed before vertical displacement reached 275 mm, which was led by the different heights of the neutral axes at the joint area and pinned supports. However, the compressive arch action was not evident in ST-M-T, because the more severe damage in the concrete slab of this specimen prevented the development of the compressive axial forces.

For the side joint specimens, as the existence of initial height difference of neutral axes in the joint area and the pinned joints, the catenary action was almost developed from the beginning. Before the fracture of the top beam flange, the internal forces in ST-S-R and ST-S-T were nearly identical. Beyond that, a higher catenary action was generated in ST-S-R, because the concrete spalling in this specimen was much

Table 3
Deformation limits and corresponding vertical loads.

Specimen	Characteristic deformation limits		
	1st peak	2st peak	Ultimate state
Steel subassembly	184kN(0.033 rad, 74 mm)	186kN(0.06 rad, 141 mm)	218kN(0.17 rad, 381 mm)
ST-M-R	324kN(0.023 rad, 52.4 mm)	288kN(0.076 rad, 171 mm)	308kN(0.216 rad, 487 mm)
ST-M-T	279kN(0.023 rad, 52.3 mm)	201kN(0.103 rad, 231 mm)	240kN(0.19 rad, 427 mm)
ST-S-R	314kN(0.068 rad, 153 mm)	310kN(0.111 rad, 250 mm)	310kN(0.17 rad, 382 mm)
ST-S-T	311kN(0.08 rad, 179 mm)	267kN(0.108 rad, 243 mm)	241kN(0.157 rad, 353 mm)

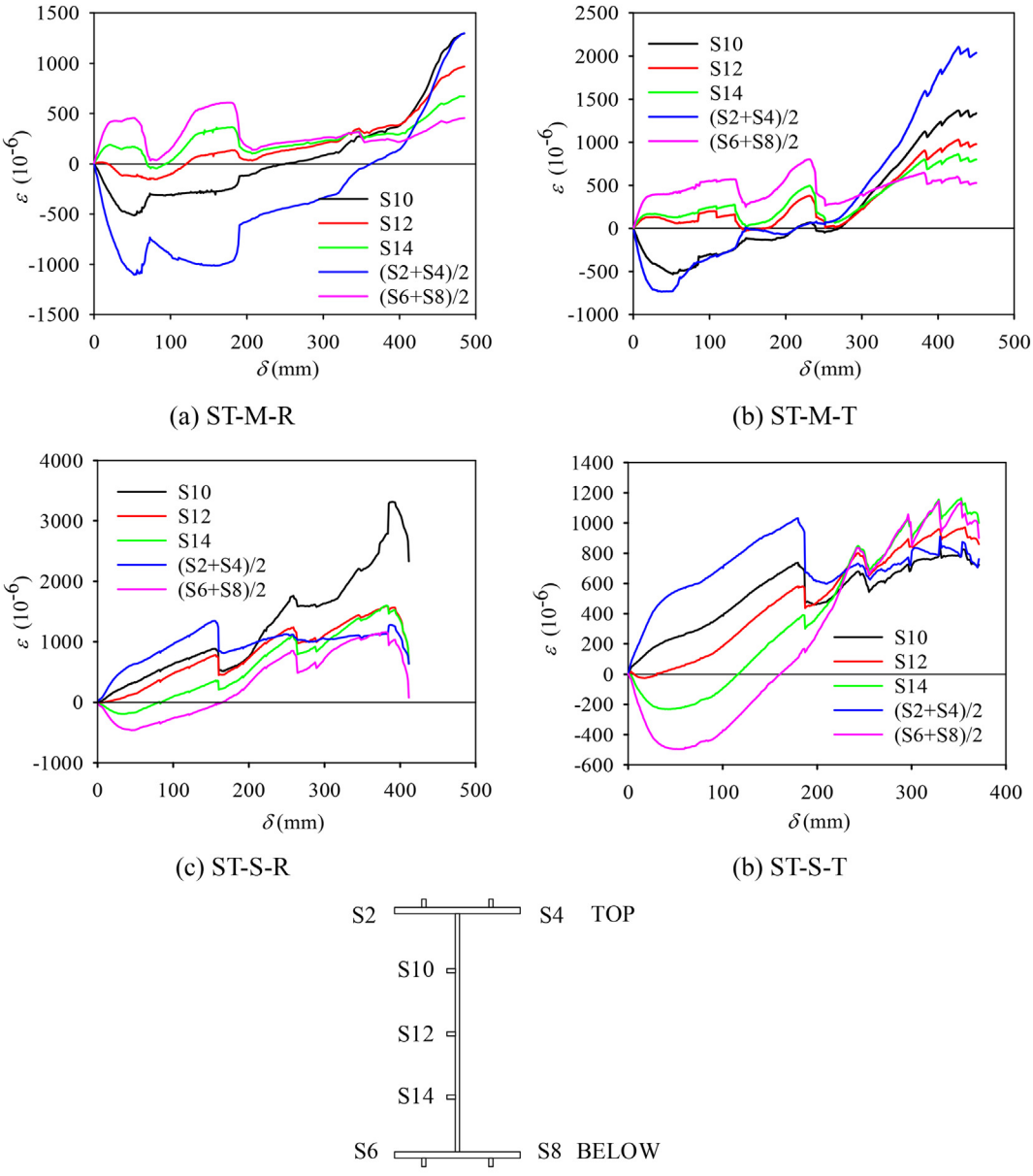

Fig. 12. Axial strain development at section E1 of specimens.

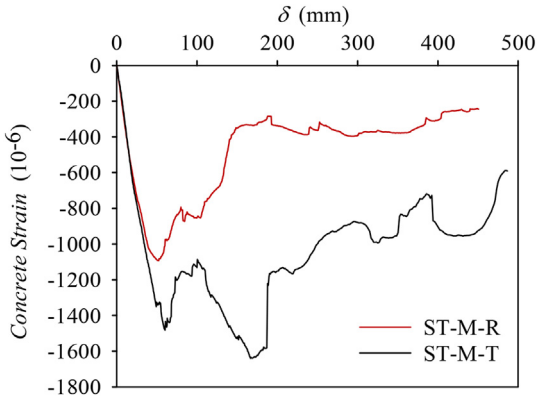

Fig. 13. Average strain of concrete at section E2 of middle joint specimens.

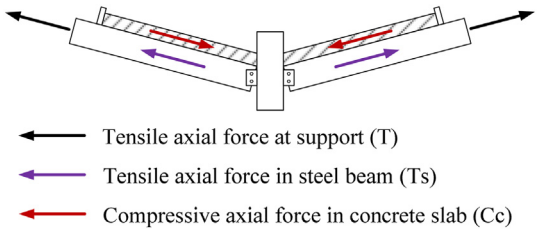

Fig. 14. Inner mechanism of catenary action.

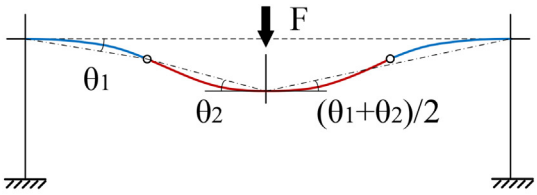

(a) Connection subassembly

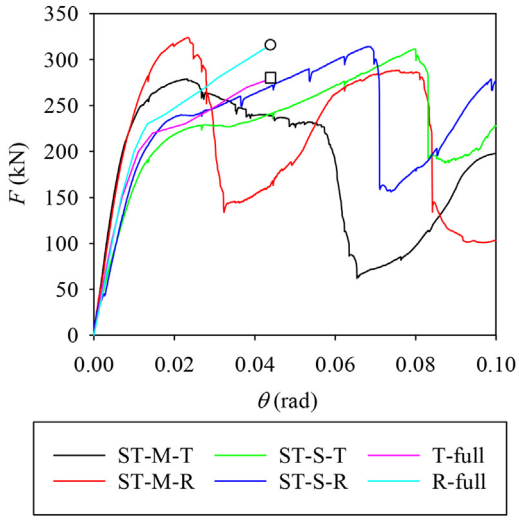

(b) Load-chord rotation angle curves

Fig. 15. Complete connection subassembly.

slight, then the steel bars in ST-S-R could generate higher tensile forces than those in ST-S-T.

4.4. Different composite floor decking

Fig. 21 shows the failure modes of cross-section profile in the middle joint specimens, from which we could find that there was more severe separation between steel deck and concrete slab in the specimen ST-M-T and ST-S-T. The reason for this is that the interlocking action resulted from inverted triangle bulges in the reentrant decking was absent

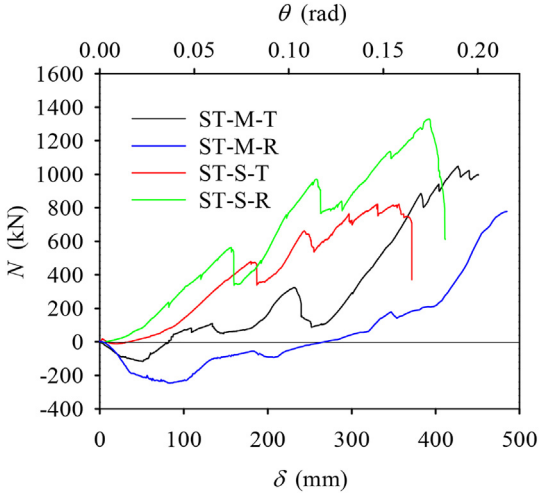

Fig. 16. Axial force development at section E1 of specimens.

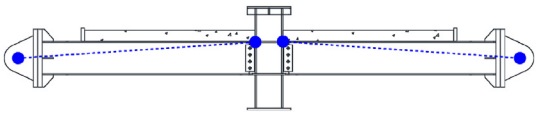

Fig. 17. Neutral axis height differences between supports and joint.

in the trapezoidal composite slabs. So that specimen ST-M-T and ST-S-T experienced a premature reduction in the composite action which caused by the separation between concrete and trapezoidal steel deck, and thus exhibited some similarity with brittle failure. When it comes to ST-M-R and ST-S-R, it shared more similarity with ductile failure due to the strong bite force among concrete and decking. At the same time, as shown in Fig. 13, the average concrete strain measured by the strain gauges also implied the influence on the composite action of different decking, which concrete strain was much higher in the specimen ST-M-R.

4.5. Dynamic response

Most progressive collapse events are usually accompanied by an obvious dynamic process. Therefore, under a sudden column loss scenario, the structural robustness evaluations need to consider the accompanied dynamic effect. With the help of the energy method proposed by Izzuddin et al. [29], the dynamic response could be calculated by the static test results based on the hypotheses that: (1)all the external energy is completely transferred into internal energy; (2)structure behaves in the same mode under dynamic and static loading. The derived dynamic response is illustrated in Fig. 22. The maximum dynamic resistances of each specimen and corresponding displacements are listed in Table 4.

Except for ST-S-T, the maximum dynamic resistances were all achieved at the flexural stage. The specimens with reentrant steel deck achieved higher dynamic resistances (242.1kN for ST-M-R and 244.0kN for ST-S-R) than the specimens with trapezoidal steel deck (232.3kN for ST-M-T and 231.1.0kN for ST-S-T). The specimens with the same steel deck achieved similar maximum dynamic resistance in middle connection and side connection. Compared with the maximum dynamic resistance of steel subassembly, the improved percentages of ST-M-R, ST-M-T, ST-S-R, ST-S-T are 62%, 56%, 63% and 55%, respectively. Considering the plan view of the prototype structure in Fig. 1, the tributary area of the middle connection and the side connection is 4.5 m × 6 m = 27 m^2. Then, the uniformly distributed load of each specimen could be calculated by dividing load F by 27 m^2, and the related results are listed in Table 4. Compared with the load combination 1.2 DL + 0.5 LL = 7kN/m^2, the improved percentage of ST-M-R, ST-M-T, ST-S-R, ST-S-T are 28.1%, 22.9%, 29.1% and 22.3%, respectively. However, the steel subassembly could only sustain 79% of the required dynamic resistance. Therefore, with the help of composite slab, the prototype building could withstand the sudden column removal.

5. Conclusions

Four composite beam-column connections with reentrant or trapezoidal decking were statically tested. The main conclusions can be summarized as follow:

(1) As noted in prior research, the progressive collapse behavior of these specimens developed flexural mechanism for smaller deformations and catenary action for larger deformations. Even though the significant catenary action was developed, the four specimens achieved their maximum resistance in the flexural stage. Specimens with trapezoidal steel deck carried at least 28% more load than the bare steel subassembly, while the specimens with reentrant steel deck increased the resistance by 44%.

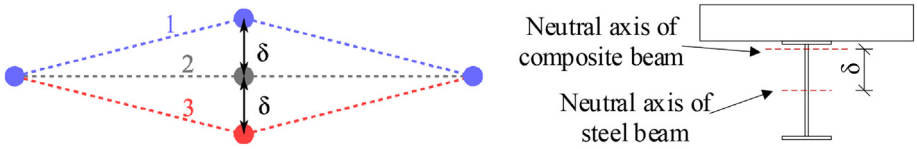

Fig. 18. Three idealistic states of neutral axis.

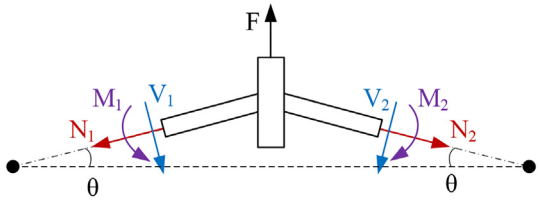

Fig. 19. Mechanical model of beam-to-column assembly.

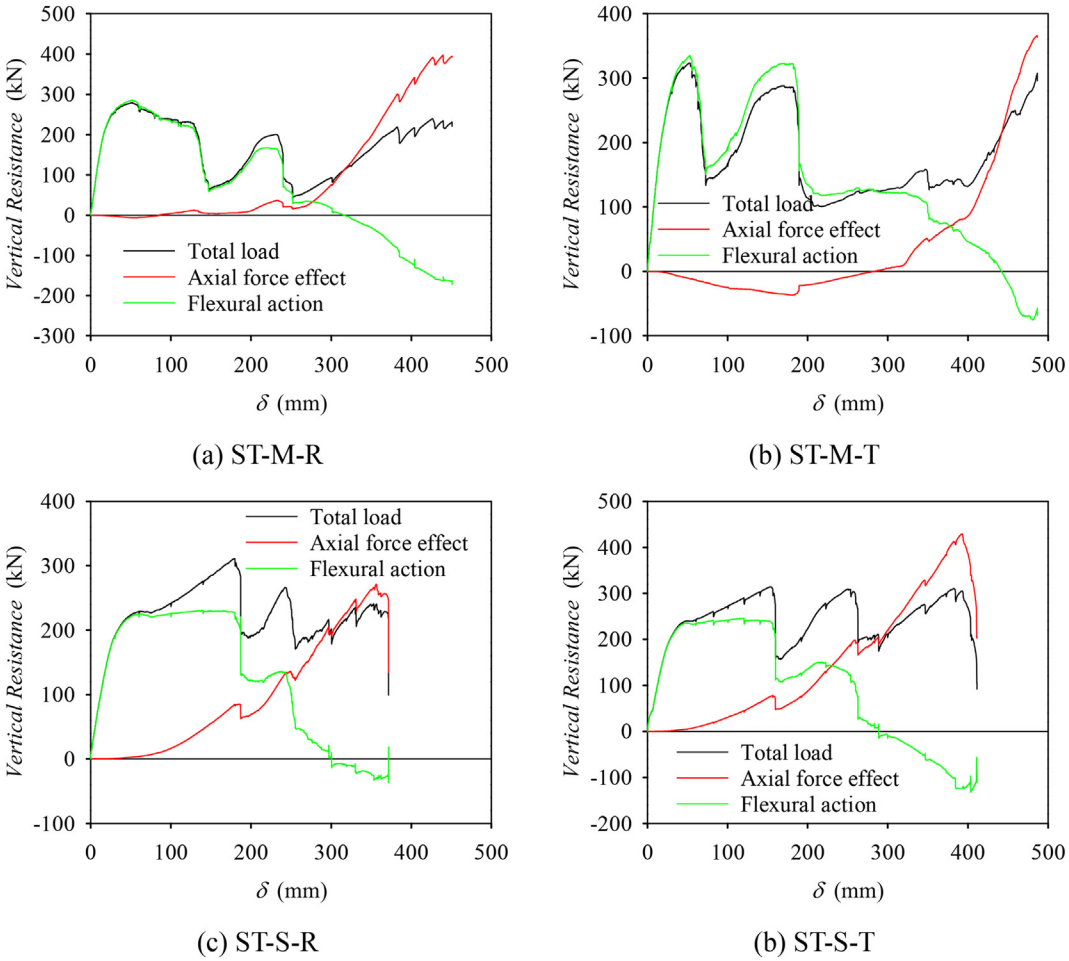

Fig. 20. Vertical resistance contributed by flexural mechanism and axial force effect.

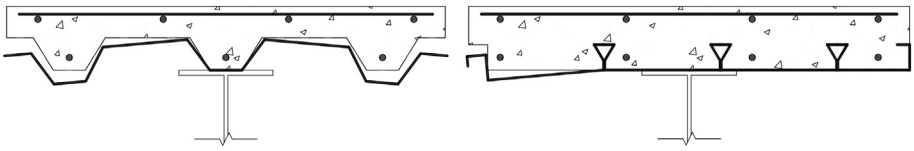

(a) ST-M-T (b) ST-M-R

Fig. 21. Comparison of composite slab failure modes.

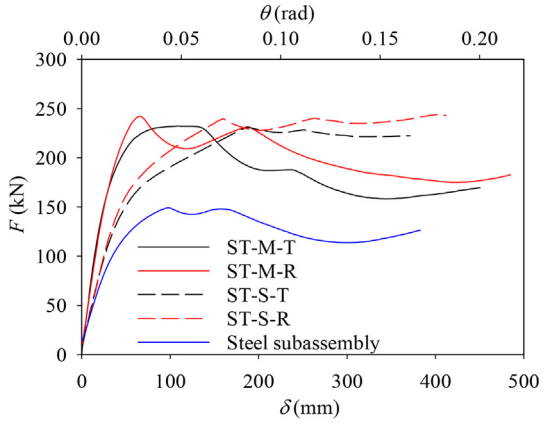

Fig. 22. Dynamic response.

Table 4
Maximum dynamic resistance and corresponding displacement.

	Maximum dynamic resistance	Corresponding displacement
Steel subassembly	149.3kN (5.53kN/m^2)	98.2 (0.044 rad)
ST-M-R	242.1kN (8.97kN/m^2)	66.1 (0.030 rad)
ST-M-T	232.3kN (8.60kN/m^2)	109.2 (0.049 rad)
ST-S-R	244.0kN (9.04kN/m^2)	403.4 (0.179 rad)
ST-S-T	231.1kN (8.56kN/m^2)	187.0 (0.083 rad)

(2) For the middle connection specimen, different steel deck has a significantly different constraint effect on the beam top flange, which leads to different plastic rotation capacity. Under the sagging moment scenario, the specimen with reentrant steel deck experienced a premature fracture but with a higher flexural resistance than that one with trapezoidal steel deck. For the side connection specimens, the influence of different steel deck on the flexural behavior is almost the same.

(3) At the large deformation stage, the separation between steel deck and concrete slab is more severe in the specimen with trapezoidal steel deck. The reinforcement in the specimens with reentrant steel deck could develop more tensile force owing to the relatively minor damage in the concrete, which benefits the development of the catenary action.

Acknowledgments

The research presented in this paper was sponsored by the Natural Science Foundation of China (NSFC) through Grant No. 51378380, “Shuguang Program” through Grant No. 15SG19 and the Sustainable Structural Engineering Research Funds from Tongji Architectural Design (Group) Co. Ltd. Any opinions, findings, conclusions, and recommendations expressed in this paper are those of the authors and do not necessarily reflect the views of the sponsors.

References

[1] U. Starossek, Progressive Collapse of Structures, Thomas Telford, London, 2009.
[2] Department of Defense (DoD), Design of Buildings to Resist Progressive Collapse: Unified Facilities Criteria UFC4-023-03. Washington (DC), 2016.
[3] General Services Administration (GSA), Alternate Path Analysis & Design Guidelines for Progressive Collapse Resistance. Washington (DC), 2013.
[4] F. Sadek, J.A. Main, H.S. Lew, S.D. Robert, V.P. Chiarito, El-Tawil S. an experimental and computational study of steel moment connections under a column removal scenario, NIST Tech. Note (2010) 1669.
[5] F. Sadek, J.A. Main, H.S. Lew, Y. Bao, Testing and analysis of steel and concrete beam-column assemblies under a column removal scenario, J. Struct. Eng. 137 (2011) 881–892, https://doi.org/10.1061/(ASCE)ST.1943-541X.0000422.
[6] B. Yang, K.H. Tan, Experimental tests of different types of bolted steel beam–column joints under a central-column-removal scenario, Eng. Struct. 54 (2013) 112–130, https://doi.org/10.1016/j.engstruct.2013.03.037.
[7] B. Yang, K.H. Tan, Robustness of bolted-angle connections against progressive collapse: experimental tests of beam-column joints and development of component-based models, J. Struct. Eng. U S 139 (2013) 1498–1514, https://doi.org/10.1061/(ASCE)ST.1943-541X.0000749.
[8] L. Li, W. Wang, Y. Chen, Y. Lu, Experimental investigation of beam-to-tubular column moment connections under column removal scenario, J. Constr. Steel Res. 88 (2013) 244–255, https://doi.org/10.1016/j.jcsr.2013.05.017.
[9] L. Li, W. Wang, Y. Chen, Y. Lu, Effect of beam web bolt arrangement on catenary behaviour of moment connections, J. Constr. Steel Res. 104 (2015) 22–36, https://doi.org/10.1016/j.jcsr.2014.09.016.
[10] X. Qin, W. Wang, Y. Chen, Y. Bao, Experimental study of through diaphragm connection types under a column removal scenario, J. Constr. Steel Res. 112 (2015) 293–304, https://doi.org/10.1016/j.jcsr.2015.05.022.
[11] X. Qin, W. Wang, Y. Chen, Y. Bao, A special reinforcing technique to improve resistance of beam-to-tubular column connections for progressive collapse prevention, Eng. Struct. 117 (2016) 26–39, https://doi.org/10.1016/j.engstruct.2016.03.012.
[12] W. Wang, C. Fang, X. Qin, Y. Chen, L. Li, Performance of practical beam-to-SHS column connections against progressive collapse, Eng. Struct. 106 (2016) 332–347, https://doi.org/10.1016/j.engstruct.2015.10.040.
[13] H. Li, X. Cai, L. Zhang, B. Zhang, W. Wang, Progressive collapse of steel moment-resisting frame subjected to loss of interior column: experimental tests, Eng. Struct. 150 (2017) 203–220, https://doi.org/10.1016/j.engstruct.2017.07.051.
[14] L. Guo, S. Gao, F. Fu, Y. Wang, Experimental study and numerical analysis of progressive collapse resistance of composite frames, J. Constr. Steel Res. 89 (2013) 236–251, https://doi.org/10.1016/j.jcsr.2013.07.006.
[15] L. Guo, S. Gao, Y. Wang, S. Zhang, Tests of rigid composite joints subjected to bending moment combined with tension, J. Constr. Steel Res. 95 (2014) 44–55, https://doi.org/10.1016/j.jcsr.2013.10.006.
[16] L. Guo, S. Gao, F. Fu, Structural performance of semi-rigid composite frame under column loss, Eng. Struct. 95 (2015) 112–126, https://doi.org/10.1016/j.engstruct.2015.03.049.
[17] B. Yang, K. Tan, Behavior of composite beam-column joints in a middle-column-removal scenario: experimental tests, J. Struct. Eng. 140 (2013) 04013045, https://doi.org/10.1061/(ASCE)ST.1943-541X.0000805.
[18] B. Yang, K.H. Tan, G. Xiong, S.D. Nie, Experimental study about composite frames under an internal column-removal scenario, J. Constr. Steel Res. 121 (2016) 341–351, https://doi.org/10.1016/j.jcsr.2016.03.001.
[19] Y. Alashker, S. El-Tawil, F. Sadek, Progressive collapse resistance of steel-concrete composite floors, J. Struct. Eng. Asce 136 (2010) 1187–1196, https://doi.org/10.1061/(ASCE)ST.1943-541X.0000230.
[20] Y. Alashker, H. Li, S. El-Tawil, Approximations in progressive collapse modeling, J. Struct. Eng. 137 (2011) 914–924, https://doi.org/10.1061/(ASCE)ST.1943-541X.0000452.
[21] E.S. Johnson, J.E. Meissner, L.A. Fahnestock, Experimental behavior of a half-scale steel concrete composite floor system subjected to column removal scenarios, J. Struct. Eng. 142 (2015) 04015133.
[22] M. Hadjioannou, S. Donahue, E.B. Williamson, M.D. Engelhardt, Large-scale experimental tests of composite steel floor systems subjected to column loss scenarios, J. Struct. Eng. 144 (2018), 04017184. https://doi.org/10.1061/(ASCE)ST.1943-541X.0001929.
[23] M. Hadjioannou, Large-Scale Testing and Numerical Simulations of Composite Floor Slabs under Progressive Collapse Scenarios, PhD Thesis 2015.
[24] Q.N. Fu, K.H. Tan, X.H. Zhou, B. Yang, Load-resisting mechanisms of 3D composite floor systems under internal column-removal scenario, Eng. Struct. 148 (2017) 357–372, https://doi.org/10.1016/j.engstruct.2017.06.070.
[25] American Society of Civil Engineers (ASCE), Minimum Design Loads and Associated Criteria for Buildings and Other Structures (ASCE7–16), Reston, Virginia, 2017.

[26] Ministry of Housing and Urban–Rural Development of the People's Republic of_ China (MOHURD), General Administration of Quality Supervision, Inspection and Quarantine of the People's Republic of China. GB: Technical Code for Application of Profiled Metal Sheets. (GB50896-2013). (GB50896–2013), 2014.
[27] Central Research Institute of Building and Construction, China Association for Engineering Construction Standardization (CECS): Technical Pecification for Welding of Stud (CECS 226:2007), 2007.
[28] W. Wang, J. Wang, X. Sun, Y. Bao, Slab effect of composite subassemblies under a column removal scenario, J. Constr. Steel Res. 129 (2017) 141–155, https://doi.org/10.1016/j.jcsr.2016.11.008.
[29] B.A. Izzuddin, A.G. Vlassis, A.Y. Elghazouli, D.A. Nethercot, Progressive collapse of multi-storey buildings due to sudden column loss— part I: simplified assessment framework, Eng. Struct. 30 (2008) 1308–1318, https://doi.org/10.1016/j.engstruct.2007.07.011.